Journal of Materials Chemistry A

ROYAL SOCIETY OF CHEMISTRY

PAPER

Published on 22 April 2026
Licensed under CC-BY 4.0

Check for updates

Cite this: *J. Mater. Chem. A*, 2026, **14**, 23441

Fe, Co, and ZIF-8 co-doped catalysts with carbon nanotubes and a SiOC composite backbone for high-temperature PEM fuel cell cathodes

Marek Mooste, *[ab] Julia Müller-Hülstede,[a] Julia G. Buschermöhle,[a] Konstantin K. Rücker,[a] Tanja Zierdt,[a] Jana Ewert,[a] Killian Fuhrmann,[a] Nils Harder,[a] Michaela Wilhelm,[c] Peter Wagner,[a] Dana Schonvogel[a] and K. Andreas Friedrich[d]

The development of high-temperature proton exchange membrane fuel cell (HT-PEMFC) technology is crucial for implementing the hydrogen economy and decarbonising (heavy) transport and aviation sectors. To replace Pt-based materials at the HT-PEMFC cathode, we propose an Fe, Co, and N-functionalised catalyst with a nanocarbon backbone consisting of a carbon nanotube (CNT) and silicon oxycarbide (SiOC) blend. SiOC is a subclass of polymer-derived carbon (PDC). The CoFe–N–CNT/PDC catalyst is prepared using zeolitic imidazolate framework-8 (ZIF-8) as a nitrogen source *via* pyrolysis, followed by an acid-leaching step. Preliminary testing of oxygen reduction reaction (ORR) activity was conducted comparatively using a rotating ring-disc electrode (RRDE) method at room temperature in 0.5 M H_3PO_4 and with a high-temperature gas diffusion electrode (HT-GDE) half-cell setup at 160 °C in conc. H_3PO_4. Comparative stability testing under RRDE and HT-GDE conditions showed the superior durability of PDC in the catalyst backbone. In more detail, a voltage loss of 36 mV was observed after a 3-hour HT-GDE test at a constant current density of 100 mA cm^{-2} for the CoFe–N–PDC catalyst, while Fe–N–C (Pajarito Powder, LLC) showed a corresponding value of 80 mV. A maximum power density (P_{max}) with CoFe–N–CNT/PDC in the HT-GDE of 187 mW cm^{-2} was obtained, outperforming the P_{max} of 153 mW cm^{-2} for Fe–N–C. During the HT-PEMFC single-cell tests, Fe–N–C with a P_{max} of 134 mW cm^{-2} surpassed the CoFe–N–CNT/PDC and CoFe–N–CNT cathodes (P_{max} of 112–124 mW cm^{-2}). The high activity towards the ORR of the CoFe–N–CNT/PDC was attributed to the presence of Fe-, Co-, and N-based active sites and an optimised nanocarbon backbone.

Received 2nd February 2026
Accepted 22nd April 2026

DOI: 10.1039/d6ta01012a

rsc.li/materials-a

1. Introduction

The development of hydrogen technologies is necessary for a clean, sustainable energy economy. It is important to deploy renewable hydrogen in areas with the greatest potential for decarbonisation, making hydrogen an ideal solution for (heavy) transportation.[1] The low-temperature proton exchange membrane fuel cell (LT-PEMFC) is a clean-energy conversion device that is already used in the automotive industry for light-duty vehicles (LDVs).[2] An attractive alternative to the LT-PEMFC is the high-temperature proton exchange membrane fuel cell (HT-PEMFC), which is better suited for heavy-duty vehicles (HDVs) and the aviation sector.[3–6] The advantages of HT-PEMFCs include the absence of liquid water, easier thermal management, a perfluoroalkyl and polyfluoroalkyl substance (PFAS)-free phosphoric-acid-doped polybenzimidazole (PA-PBI) membrane, high resistance to CO impurities, and the possibility to use syngas as fuel.[7–10]

Currently, Pt-based nanocarbon (Pt/C) materials are used for oxygen reduction reaction (ORR) electrocatalysis at the cathodes of LT- and HT-PEMFCs, which hinders the widespread use of these devices. The main Pt/C-specific problems in HT-PEMFCs are the high cost and scarcity of Pt, lower durability compared to LT-PEMFCs, and Pt poisoning by phosphate anions from the PA-PBI membrane, necessitating impractically high catalyst loadings.[6,11–13] As one possible approach to mitigate the poisoning problem of Pt and to increase the activity towards the ORR under HT-PEMFC conditions, the incorporation of transition metal (TM, *e.g.*, Co, Ti, and Fe) compounds with Pt/C catalysts has been successfully performed in several studies.[14–16] Furthermore, to completely avoid the use of

[a]*Institute of Engineering Thermodynamics, German Aerospace Center (DLR), Carl-von-Ossietzky-Str. 15, 26129 Oldenburg, Germany*

[b]*Institute of Chemistry, University of Tartu, Ravila 14a, 50411 Tartu, Estonia. E-mail: marek.mooste@ut.ee; Tel: +372 737 5177*

[c]*Advanced Ceramics, University of Bremen, Am Biologischen Garten 2, IW3, 28359 Bremen, Germany*

[d]*Institute of Engineering Thermodynamics, German Aerospace Center (DLR), Pfaffenwaldring 38-40, Stuttgart, 70569, Germany*

platinum-group-metal (PGM)-based catalysts at the HT-PEMFC cathode, the development of transition metal–nitrogen–carbon (M–N–C) materials has attracted increased attention.[17–19]

The primary issues of M–N–C under acidic HT-PEMFC conditions are demetallation, nitrogen protonation, and carbon oxidation, all of which contribute to poor long-term durability of ORR electrocatalysts at the cathode.[20,21] Durability becomes particularly important for HDV applications due to the extended driving lifetime.[2] The most studied non-PGM materials for HT-PEMFC cathodes are currently Fe–N–C, whose durability issues are caused by oxidation of carbon in an acidic environment and the demetallation of nitrogen-coordinated iron (Fe–N_x) active sites for the ORR by O_2 itself. Additionally, both processes are facilitated by reactive oxygen species (ROS), which form due to the presence of Fe^{2+} catalysing the Fenton reaction.[22] Therefore, scavenging ROS or M–N–C modification to prevent ROS formation is needed, *e.g.*, *via* incorporating additional TMs into the Fe–N–C composition.[23,24] The construction of bimetallic M–N–C (*e.g.*, Fe/Co, Fe/Mn, and Fe/Cu) materials can effectively improve the catalyst's stability and activity towards the ORR.[25–27] These M–N–C materials contain bimetallic sites that exhibit a synergistic effect, which facilitates ORR kinetics by significantly increasing the binding energy of ORR intermediates and lowering the ORR activation energy barrier.[21,28]

Among bimetallic M–N–C materials, the Fe and Co combination is known to provide increased stability for ORR catalysts under acidic conditions as strong interaction between Fe–N_x and Co–N_x could stabilise the catalyst against migration and agglomeration.[29,30] Also, Fe–N_x, Co–N_x and Fe/Co–N_x are known to exhibit high electrocatalytic activity towards the ORR.[31–34] For example, different CoFe–N–C cathode equipped anion exchange membrane fuel cells (AEMFCs) have shown very good performance in tests with a peak power density (P_{max}) of 0.5–1.0 W cm^{-2}.[35–37] Also, the Fe and Co combination was found to be optimal for the HT-PEMFC cathode in a recent investigation, where Fe/Co, Fe/Cu, and Fe/Mn bimetallic M–N–C catalysts were compared.[38]

The development of extremely robust catalytic supports suitable for the harsh HT-PEMFC environment is very important.[18] In numerous studies, the polymer-derived carbon (PDC) subclass silicon oxycarbide (SiOC) has been shown to be suitable as a M–N–C support material due to its high chemical and thermal stability, *e.g.*, for AEMFCs and zinc–air batteries (ZABs).[39–42] For the HT-PEMFC cathode application, the relatively low specific surface area (SSA) of SiOC was found as one shortcoming limiting the high density of active sites for the ORR.[38,43] Multi-walled carbon nanotubes (CNTs) meet the stability criteria for HT-PEMFC conditions, exhibit high corrosion resistance, and could also increase the SSA.[44,45] Therefore, combining CNTs and PDC into the M–N–C backbone could yield a composite nanocarbon that is suitable for the HT-PEMFC cathode.

In the present investigation, various binary TM and N co-doped PDC/CNT composite M–N–C materials were prepared for the HT-PEMFC cathode. Zeolitic imidazolate framework-8 (ZIF-8) from the previous investigation was used as the N-source.[38] The preliminary electrocatalyst ORR activity evaluation was performed comparatively in two systems: a rotating ring-disc electrode (RRDE) at room temperature (RT) and a high-temperature gas diffusion electrode (HT-GDE) half-cell setup at 160 °C. Based on the HT-GDE results, whose testing conditions most closely match the target application, the Co- and Fe-containing N-doped PDC/CNT and CNT catalysts were ultimately employed at the HT-PEMFC cathode with a commercial Fe–N–C catalyst (Pajarito Powder, LLC) as a comparison.

2. Experimental

2.1. Catalyst material synthesis

The nanocarbon supports used in the present investigation were CNTs (multi-walled carbon nanotubes 95%, OD: 10–30 nm, L: 5–15 μm, CP-0006-SG, IoLiTec Ionic Liquids Technologies GmbH) and SiOC-based PDC developed in previous work.[38,39] The preparation route of PDC is given in Section S1 of the SI. Specific nanocarbons or their 1 : 1 blend were mixed with ZIF-8 (Basolite® Z1200, Sigma-Aldrich) and TM salts in methanol (99.9%, Thermo Scientific Chemicals) by ultrasonication for 2 hours followed by evaporating the solvent at 60 °C in an oven. The TM salts used in various combinations were iron(II) acetylacetonate (FeAcac, 95%, abcr GmbH), manganese(II) acetylacetonate (MnAcac, Sigma Aldrich), and cobalt(II) acetylacetonate (CoAcac, Sigma Aldrich). The specific amounts (wt%) of used precursors and the final catalyst designations are given in Table S1. The pyrolysis of the dried mixture was performed in a N_2 environment at 950 °C with a dwelling time of 1 h according to the previously optimised procedure.[38] Similarly, the 16-hour acid leaching procedure at 90 °C in 2 M H_2SO_4 (96%, Merck)[46,47] was applied to all of the prepared catalysts, which was previously found to be beneficial for HT-PEMFC cathodes of M–N–C type.[38] The acid leaching was performed with *ca.* 50 mg of catalyst in *ca.* 50 mL of acid solution on a stovetop with a magnetic stirrer (400 rpm) and using a condenser. After leaching, the catalyst was filtered with a polyethersulfone filter (pore size 0.22 μm) by washing with MilliQ water until pH = 7 was obtained, dried at 60 °C, and subjected to second pyrolysis under the very same conditions as the first pyrolysis. The outline of the preparation route for the CoFe–N–CNT/PDC catalyst material is depicted in Scheme S1.

2.2. Physical characterisation

Scanning electron microscopy with energy-dispersive X-ray spectroscopy (SEM-EDS) analyses were carried out on gold-sputtered (48 seconds) M–N–C powders prepared with the sputtering machine Sputter Coater 108 Auto (Cressington). The SEM experiments were conducted with a SUPRA 40 (Zeiss) equipped with an SE2 detector for the images and an XFlash 6|30 (Bruker) detector for the EDS. Nitrogen adsorption–desorption experiments at 77 K were performed using a Belsorp-Mini (Bel Japan Inc.) to determine the SSA *via* the Brunauer–Emmett–Teller (BET) method. M–N–C powders (particle size < 300 μm) were pre-conditioned under vacuum at 200 °C for 24 h prior to the measurements.

 This journal is © The Royal Society of Chemistry 2026

Raman spectroscopy measurements were performed using a Horiba LabRAM Aramis. A 532 nm laser with a power of 5 mW, a 300 g mm^{-1} grating, and an objective with 50× magnification was used. The data were collected with 120 acquisitions at an integration time of 2s. The X-ray diffraction (XRD) analysis was performed using a Bruker D8 Advance diffractometer with a Ni-filtered Cu Kα radiation source and a LynxEye line detector. The diffraction patterns were collected with a 0.013° 2θ step from 5° to 89°, with a counting time of 534 s per step. The description of inductively coupled plasma mass spectrometry (ICP-MS) measurements is provided in Section S2.

High-resolution transmission electron microscopy (HR-TEM) data were collected with a Jeol 2100F S-TEM device (magnification: 50× to 1 500 000×; acceleration voltage: 80–200 kV). EDS measurements were performed with an Oxford AZTEC EDX-system with an SDD detector (X-Max80, 80 mm^2 detector area, resolution 129 eV (Mn K), and 1 million counts per sample). The samples for HR-TEM and EDS were prepared by suspending 2–5 mg of M–N–C powder in 5 mL of ethanol and sonicated for 30 minutes. 2 × 5 μl of suspension was dropped on a TEM grid and dried in air at RT.

For X-ray Photoelectron Spectroscopy (XPS) analyses, an ESCALAB 250Xi (Thermo Fisher) with monochromatic Al-Kα radiation and a beam diameter of 650 μm was used. For the survey spectra, three scans were recorded using a transit energy of 100 eV, a dwell time of 20 ms, and a step size of 1 eV. High-resolution XP spectra for the elements C (1s, 3 scans), O (1s, 5 scans), N (1s, 10 scans), Si (2p, 10 scans), Fe (2p, 15 scans), Co (2p, 15 scans) and Zn (2p, 3 scans) were recorded with a transit energy of 20 eV, a dwell time of 50 ms and a step size of 0.02 eV. For peak fitting, the software Avantage™ V6 (Thermo Fisher) was used, utilising a smart background and a Gauss–Lorentz line shape.

2.3. RRDE and HT-GDE half-cell studies

The specific details for ORR studies with the RRDE method at RT and HT-GDE half-cell setup tests at 160 °C are given in Section S3.

2.4. HT-PEMFC testing

A HT-PEMFC single cell test station from Schubert GmbH equipped with a quickCONNECTfixture (qCF 5/100 HT, balticFuelCells) was employed. The fabrication route for the membrane electrode assembly (MEA) and HT-PEMFC test protocols were adapted from recent investigations.[38,48] Three cathode catalysts (Fe–N–C (PMF-011904, Pajarito Powder, LLC), CoFe–N–CNT/PDC, and CoFe–N–CNT) were investigated using the same gas diffusion layer (GDL), ink composition, and drop casting technique as those used for the HT-GDE tests (Section S3) with a final M–N–C loading of 3.5 ± 0.1 mg cm^{-2} (confirmed by ICP-MS). The cathode, a PA-PBI membrane (Celtec®-P, BASF, pre-soaked in 50% H_3PO_4 for 24 h), and a commercial Celtec®-based Pt/C anode (0.86 mg_{Pt} cm^{-2}) were sandwiched by hot pressing (1.0 kN for 30 s at 140 °C) using TRG 2 pneumatic lab presses (Paul-Otto Weber GmbH) into a 4.05 cm^2 MEA outlined with Kapton® frames. Prior to pressing, the thickness of every MEA component was measured with a digital thickness dial gauge (Käfer Messuhrenfabrik GmbH & Co. KG), and stainless-steel shim shields with 80% of the total thickness of all MEA components were used to prevent over-crushing of the MEA. The pressing was followed by thermal annealing in air at 160 °C for 30 min in an FD 53 drying and heating oven with forced convection (BINDER GmbH). The MEA performance was evaluated with a cell compression of 0.75 MPa in a cell fixture cF5/100 HT Gr V1.4 with serpentine graphitic flow fields (balticFuelCells). After the gas tightness test with N_2, the gases were switched to dry H_2/O_2 (stoichiometry 1.5/9.5) at a constant load of 100 mA cm^{-2}. After reaching 160 °C, a galvanostatic polarisation curve was recorded. Next, an external potentiostat, Modulab2100A (Ametek), equipped with a booster (12 V/20 A), was connected to the cell for electrochemical impedance spectroscopy (EIS) and cyclic voltammetry (CV). The EIS was recorded in a frequency range of 100 kHz to 100 mHz at a fixed current density of 0.1 A cm^{-2} with an amplitude of 10 mV r.m.s. and an equilibration time of 5 min. The CV testing was performed at a N_2 flow rate of 0.1 L min^{-1} at the cathode and a H_2 flow rate of 0.1 L min^{-1} at the anode.

3. Results and discussion

3.1. Physical characterisation of the catalysts

As one of the main aims of this paper was the investigation of the nanocarbon (composite) backbone influence on the ORR activity of the CoFe–N–C catalyst, corresponding materials with various nanocarbon structures and their precursors were subjected to physical characterisation. The Raman spectrum of the pristine CNTs exhibits the characteristic peaks of D (1335 cm^{-1}), G (1565 cm^{-1}), and D2 (2670 cm^{-1}) inherent to the spectra of multi-walled carbon nanotubes (Fig. 1a).[49,50] The G band corresponds to the graphite (common to all sp^2 systems), D conforms to structural defects or contaminants, and 2D corresponds to the second-order Raman scattering process, which is known as an overtone of the D mode. The degree of graphitization (I_D/I_G ratio) indicates that the pristine CNTs are already rather defective, and pyrolysis with ZIF-8, metal precursors, and PDC does not significantly affect the already highly defective carbon structure according to Raman spectroscopy data. In the case of precursor CNT-free material, CoFe–N–PDC, the Raman signals (D, G, and 2D) very likely originate from the carbon structure formed during the pyrolysis of ZIF-8 and TM acetylacetonates as these peaks are absent in the pristine PDC. This is also supported by the visibly broader G band and the weaker 2D band, which are characteristic of functionalised materials and amorphous carbon.[51] Furthermore, the Raman spectrum of CoFe–N–PDC is also very similar to the ones of binary TM containing PDC catalysts functionalised with N using dicyandiamide (DCDA) in our parallel investigation for ZAB application.[39] This indicates that the carbon formed during the pyrolysis of ZIF-8 and DCDA with TM species could exhibit a similar structure, *e.g.*, the formation of CNTs is well documented for both N sources.[39,52–54]

N_2 adsorption–desorption studies (Fig. 1b and Table 1) show that the inclusion of CNTs could be beneficial for increasing the

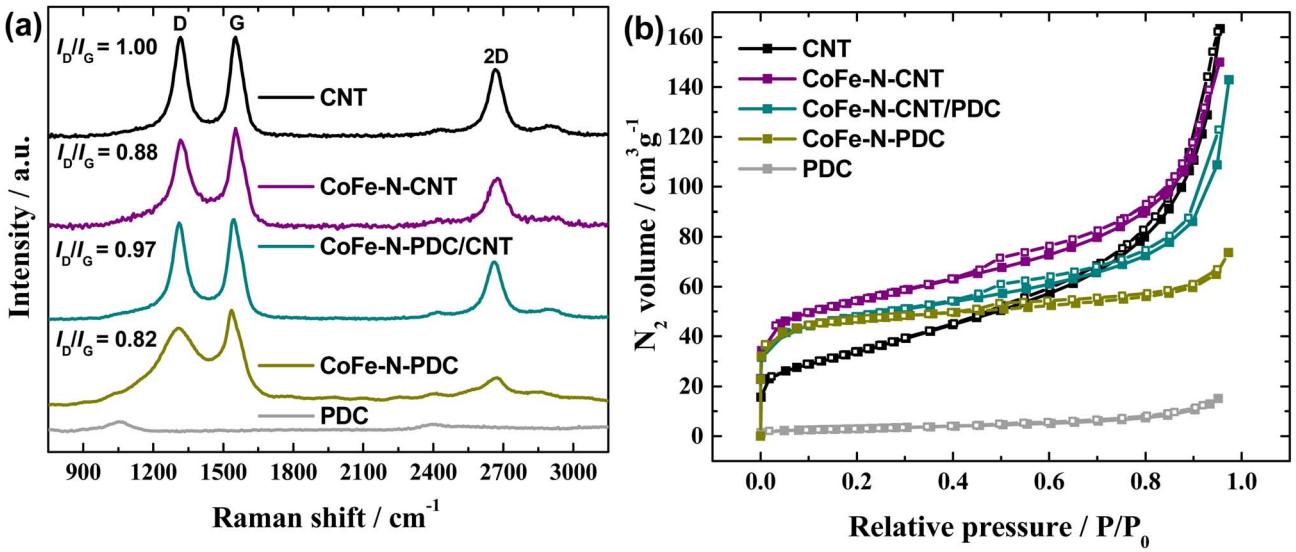


Fig. 1 (a) Raman spectra and (b) N_2 adsorption–desorption isotherms for different catalyst materials. (■) Adsorption and (□) desorption measurement points.

SSA of the catalyst, as the difference in BET surface area (S_{BET}) between PDC and CNT precursors is 10×. Concurrently, the S_{BET} value for both CoFe–N–C materials with PDC and the CNT/PDC backbone is very similar, *ca.* 177 m^2 g^{-1}, while only in the case of CoFe–N–CNTs, the highest S_{BET} of *ca.* 200 m^2 g^{-1} is obtained. This indicates that the pyrolysis of ZIF-8 with TMs creates additional nanocarbon materials (*e.g.* CNTs)[38,40] with considerable contribution to the overall SSA. Both CNT-containing CoFe–N–C samples exhibit type IV isotherms with a hysteresis loop, indicating micro-mesoporous materials. The mesopores are necessary to ensure the mass transport of O_2 molecules and electrolyte access, while micropores could provide a high density of ORR active sites.[55,56] Moreover, the lower d_p value for all CoFe–N–C compared to the precursor materials refers to micropore formation due to the evaporation of Zn during pyrolysis as is known for ZIF-8 containing catalysts.[57] Altogether, all CoFe–N–C materials prepared herein could host a higher number of active sites for the ORR according to the S_{BET} value compared to the CoFe–N–SiOC (S_{BET} = 132 m^2 g^{-1}) from previous work[38] indicating a more promising ORR catalyst design.

The XRD patterns in Fig. 2a and b are divided into PDC- and CNT-containing materials, respectively, along with the specific backbone precursors, to better understand the influence of the carbon composite components. First, the graphite (IMERYL Graphite & Carbon) powder in the PDC composition yields a very intense XRD reflex (Fig. S1), which suppresses all less intense reflexes similarly to the previous investigation.[38] Therefore, the carbon reflexes at 26–26.5° in Fig. 2 are shown out of scale. In the case of all CoFe–N–C materials, the reflex for the FeCo alloy is registered with the strongest reflex at *ca.* 45° similarly to the previous investigations of different M–N–C catalysts with the Fe and Co combination.[38,58,59] In the case of CNTs and CNT-based catalysts (Fig. 2b), the XRD reflexes of molybdenum carbides (Mo_2C and MoC) are observed, which are very likely the residues from the preparation of CNTs (CP-0006-SG, IoLiTec) by the chemical vapour deposition method.

The SEM and TEM images of the CoFe–N–C catalysts (Fig. 3) revealed the morphology of the various nanocarbon composite backbones. The CNTs are observed in the case of all catalyst materials, whereas in the case of CoFe–N–PDC they have formed *in situ* during the pyrolysis of the ZIF-8 precursor with TMs as is also known from several previous investigations.[38,40,52,53,60] The observable difference is that in the case of CoFe–N–PDC, a lower overall amount of CNTs with a smaller diameter is observed. This observation suggests that the addition of CNTs is a beneficial direction in optimising nanocarbon structures for ORR catalysts. The bulk composition of the CoFe–N–C catalysts according to the EDS studies (Table 2) showed the expected presence of N around 4 at% in all the catalysts together with 0.25–0.50 at% of total Co and Fe necessary for M–N_x formation with high ORR electrocatalytic activity.[21,60] The content of Si is in

Table 1 Textural properties of different catalyst materials shown in Fig. 1b, monolayer volume (V_m). BET surface area (S_{BET}), total pore volume (V_{tot}) and mean pore diameter (d_p)

	PDC	CNTs	CoFe–N–CNTs	CoFe–N–CNT/PDC	CoFe–N–PDC
V_m/cm^3 g^{-1}	2.45	27.7	45.8	40.6	40.8
S_{BET}/m^2 g^{-1}	10.67	120.5	199.1	176.6	177.5
V_{tot}/cm^3 g^{-1}	0.023	0.252	0.232	0.221	0.114
d_p/nm	8.77	8.39	4.66	5.01	2.57

 This journal is © The Royal Society of Chemistry 2026

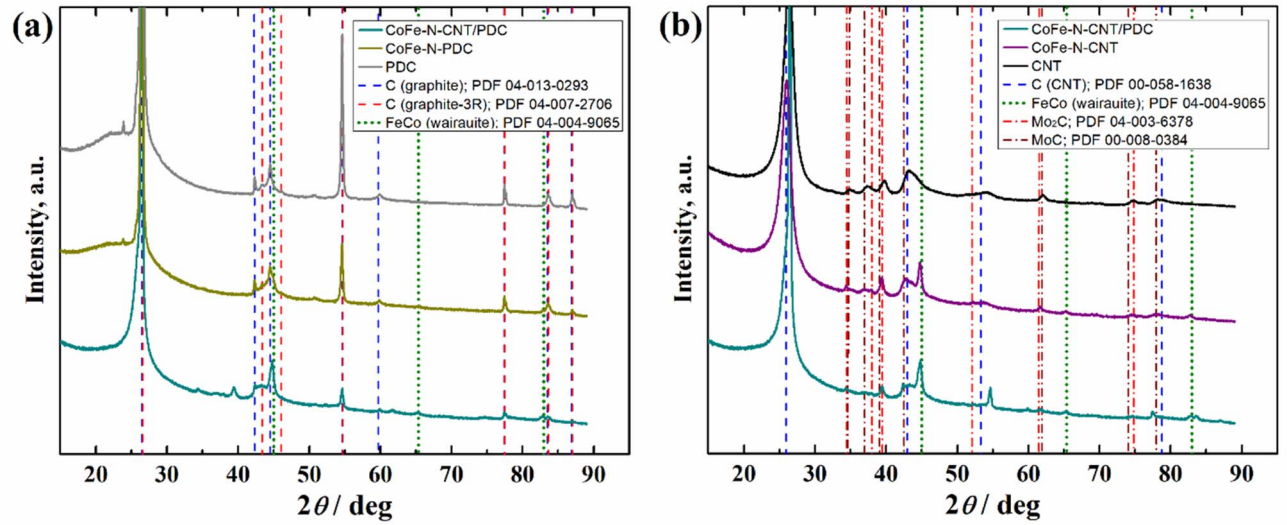


Fig. 2 XRD patterns for different catalyst materials and their backbone precursors for (a) PDC- and (b) CNT-containing materials.

accordance with the various amounts of PDC in the nanocarbon backbone, while trace amounts of Zn were also observed specifically in the case when PDC is used. Since the determination of Mo content was not feasible due to the technical limitations (Au support) and the uncertainty values for TMs were considerable, ICP-MS analyses were performed to

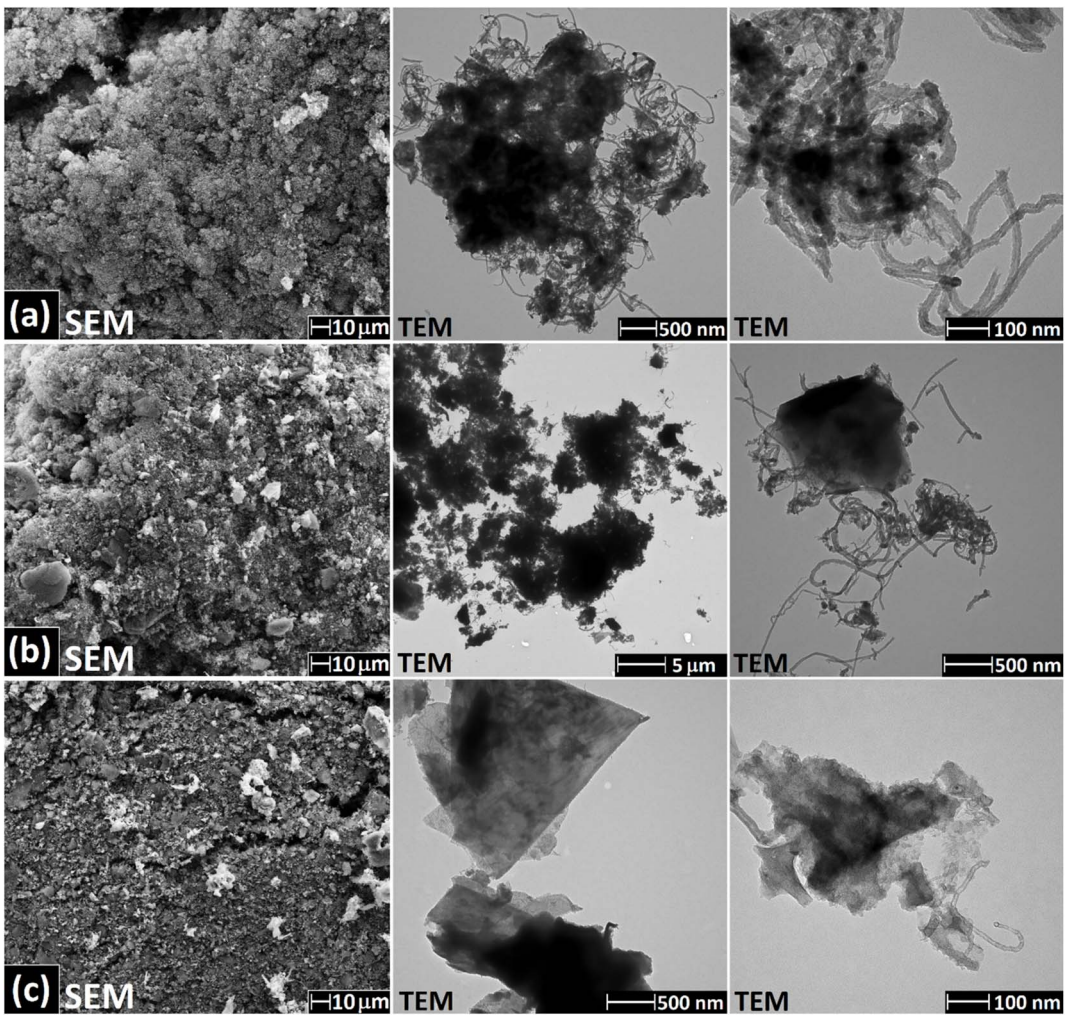


Fig. 3 SEM and TEM images of (a) CoFe–N–CNTs, (b) CoFe–N–CNT/PDC, and (c) CoFe–N–PDC catalysts.

Table 2 Elemental composition (at%) determined from EDS analysis for different nanocarbon backbone CoFe–N–C catalysts

Element	CoFe–N–CNT	CoFe–N–CNT/PDC	CoFe–N–PDC
C	91.62 ± 0.68	88.32 ± 1.78	77.27 ± 1.37
N	4.63 ± 0.40	3.66 ± 0.76	4.37 ± 0.60
O	3.12 ± 0.51	5.53 ± 1.33	13.12 ± 1.08
Si	—	1.75 ± 0.51	4.98 ± 0.98
S	0.32 ± 0.07	0.24 ± 0.06	0.01 ± 0.02
Fe	0.17 ± 0.04	0.22 ± 0.11	0.15 ± 0.06
Co	0.15 ± 0.06	0.28 ± 0.22	0.10 ± 0.06
Mo	n.d.	n.d.	n.d.
Zn	—	0.01 ± 0.01	0.02 ± 0.03

study the TM and S content with higher precision (Table S2). The Fe, Co, Zn, and S content shows similar trends among the ICP-MS and EDS investigations, whereas the contents of Mo and S are directly dependent on the CNT amount, indicating the origin of these elements from CNTs.

To study the structure and elemental distribution in the CoFe–N–C catalysts in more detail, the HR-TEM images were collected, and the elemental mapping was performed (Fig. 4 and S2, S3). The HR-TEM images reveal the fine distribution of N and the presence of TM nanoparticles in the structure of all the catalysts. More specifically, the CoFe alloy nanoparticles are observed as the maps of the corresponding elements are overlaid and the XRD analysis revealed the reflex corresponding to the very same alloy (Fig. 2). Furthermore, the overlay of Fe and Co elemental maps could indicate the presence of Co and Fe bimetallic sites, which are highly beneficial for ORR activity.[21] In the mapping images, the Mo nanoparticles are clearly observed in the case of CoFe–N–CNTs (Fig. S2b), while their location distinctly varies from those of CoFe. This indicates that Mo is probably a residue from the commercial CNT (CP-0006-SG, IoLiTec) fabrication procedure with relatively thick carbon coating as only the XRD reflexes for molybdenum carbide were observed (Fig. 2b). Also, the CoFe alloy nanoparticles in the catalyst materials are covered with several graphene layers (Fig. 4a), which explains their preservation after the harsh acid treatment procedure in 2 M H_2SO_4 for 16 h.

XPS studies were performed to investigate the surface composition of the Fe–N–CNT/PDC and various CoFe–N–C catalysts (Fig. 5). From the surface of all the catalyst materials, the XP signals for Fe 2p, O 1s, N 1s, and C 1s were detected. Additionally, in the case of PDC and Co salt used in the catalyst precursor mixture, the XP signals from Si 2s/2p and Co 2p, respectively, were detected. No clearly distinguishable photoelectron signal for Zn over the background was detected due to the acid leaching and second pyrolysis effect known for its removal.[38,57,61,62] Additionally, no distinct XP signals for the S or Mo were detected, indicating that these elements originate from the inside of commercial CNTs (Tables 2 and S2) and are not present within the 5–10 nm depth[63] of the catalyst surface. The C 1s XPS peak (Fig. S4) mainly corresponds to the graphitic carbon (C=C sp^2, *ca.* 284.4 eV)[64,65] in the case of all materials, which is supported by the XRD and Raman spectroscopy results

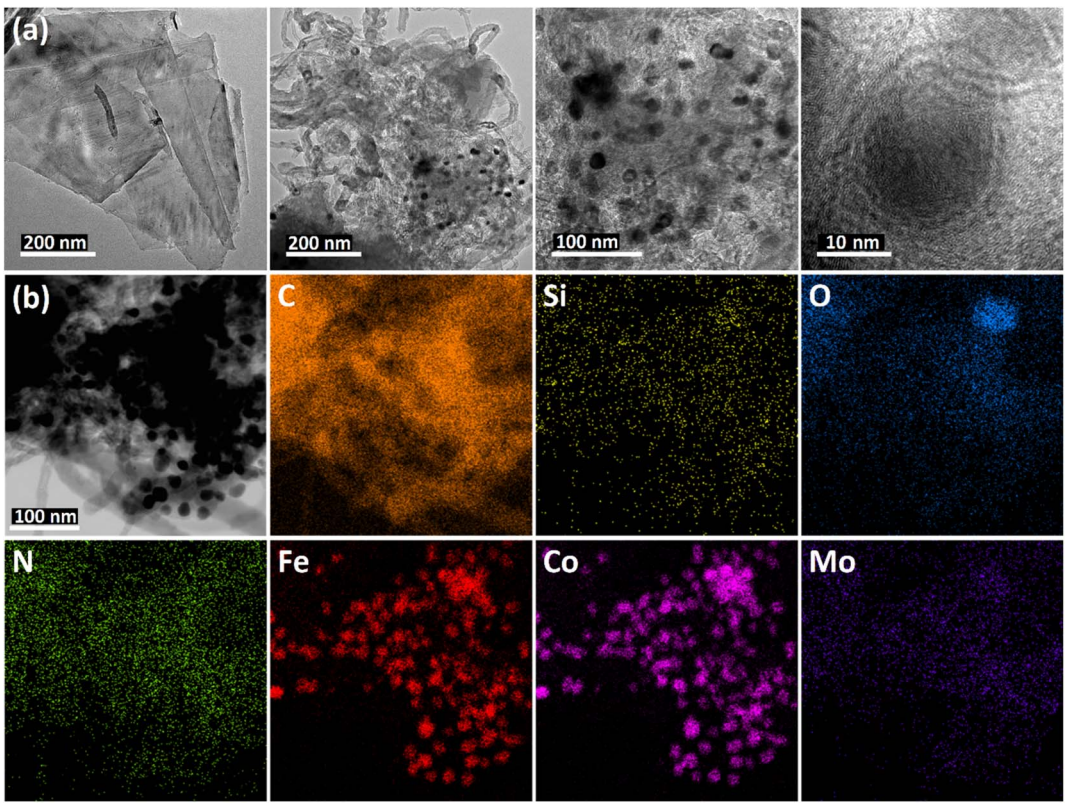


Fig. 4 Bright-field HR-TEM images for the CoFe–N–CNT/PDC catalyst at (a) different magnifications and locations and (b) with TEM-EDS elemental maps.

 This journal is © The Royal Society of Chemistry 2026

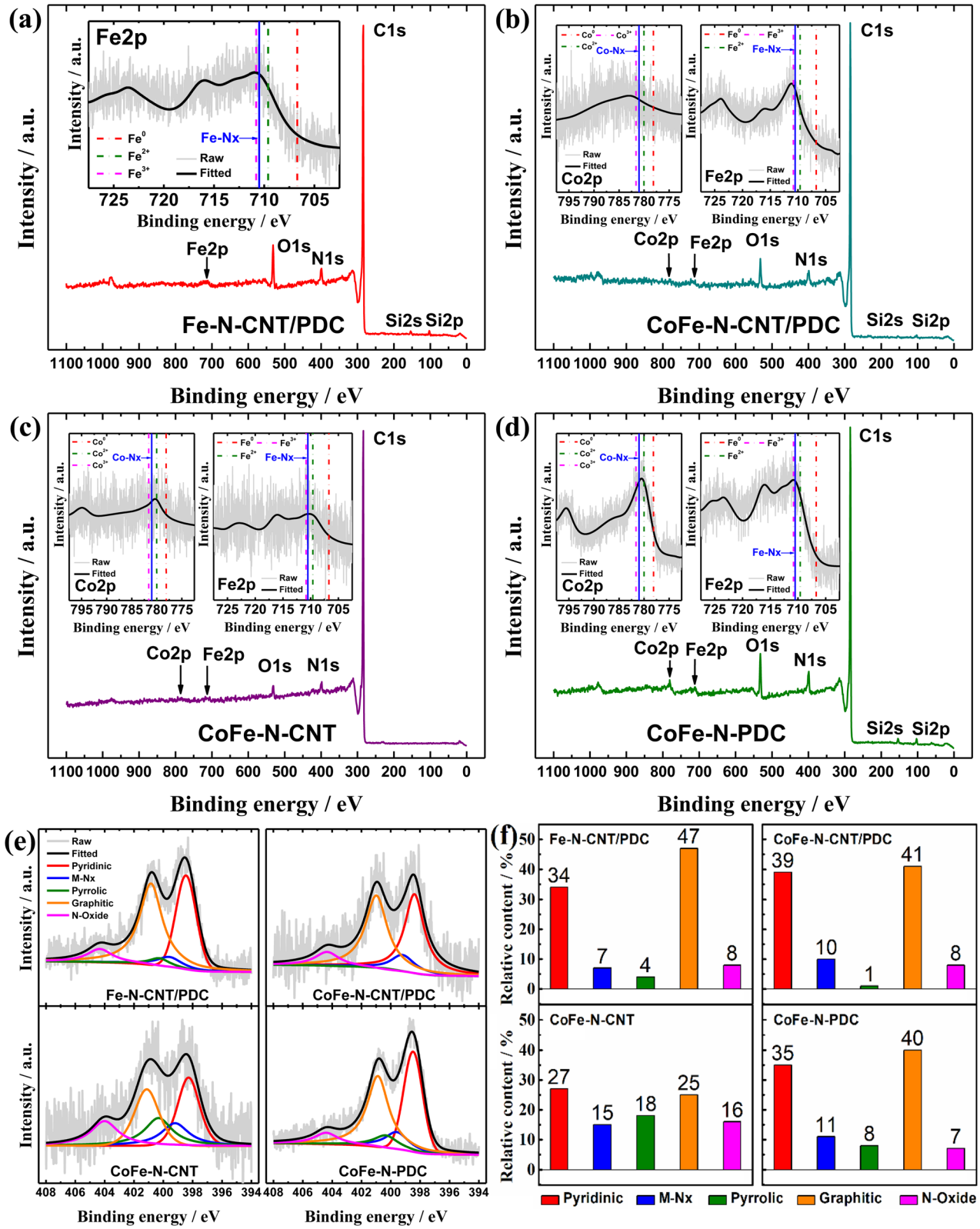


Fig. 5 (a–d) Survey XP spectra and high-resolution Fe 2p and Co 2p XPS spectra with indicated peak maxima of the respective oxidation states, and (e and f) high-resolution N 1s XPS spectra and relative content (rounded to an integer) of the determined nitrogen species for different M–N–C catalyst material powders.

(Fig. 1a, 2 and S1) together with previous reports for various SiOC,[42,66] ZIF-8,[67,68] and CNT-based[69,70] catalysts prepared *via* pyrolysis. The highly graphitic carbon skeleton provides good electrical conductivity to the active sites for the ORR.[71] As expected, the amount of PDC in the nanocarbon backbone is in correlation with the higher amount of C–O (*ca.* 286.2 eV) and C=O (*ca.* 287.3 eV) bonds in the C 1s spectrum originating from the SiOC structure in the case of CoFe–N–C catalysts (Fig. S4).

The deconvolution of N 1s spectra into 5 different N species can provide important information about the presence of the active sites for the ORR in the catalysts (Fig. 5e and f).[38,72] As a common observation among all materials, the highest relative content is observed for pyridinic-N (27–39%, *ca.* 398.3 eV) and graphitic-N (25–47%, *ca.* 401.0 eV). These two N species are considered the most important for providing high activity towards the ORR, as the pyridinic-N with a lone pair of electrons can favour the adsorption of O_2 or OOH and graphitic-N enhances the electronic conductivity.[68,73,74] Furthermore, the pyrrolic-N (*ca.* 400.3 eV) and especially M-N_x (*ca.* 399.2 eV)[29,32,75,76] species are also of utmost importance, as due to their close binding energy peak values and peak overlapping, they are very difficult to be clearly distinguished from each other. For example, in the investigation of dual TM catalyst FeCu–N–C by Hao *et al.*,[77] the admirable ORR activity and stability were mainly attributed to the pyrrolic-N-type of Fe–N_4 sites. To further evaluate the presence of M–N_x sites in the (Co)Fe–N–C materials prepared herein, high-resolution XP spectra in Fe 2p and Co 2p regions were recorded and studied (Fig. 5a–d and S5). Due to the modest Fe/Co bulk content (Table 2) and acid leaching procedure, the weak XP signals of these TMs are collected from the catalyst surface with a low signal-to-noise ratio (SNR). Therefore, determining the surface metal content (at%) is not adequate due to the SNR's influence on the deconvolution procedure (Fig. S5).[78,79] In this situation, it is feasible to determine the locations of the maxima for the Fe and Co XP peaks with different oxidation states, which have been cross-checked with literature sources (Fig. 5a–d).[38,48] It can be concluded that the Fe and Co atoms on the material surface are rather in oxidation states (+II/+III) and not metallic (0). This is supported using a strong acid treatment, which can oxidise any 0-valent TM and wash the TM species away from the surface and outside of the graphitic layer-protected TM nanoparticles (Fig. 4 and S2, S3).[80] The M–N_x species are known to be resistant to acid leaching[81] and the XP peak maxima in Fe 2p and Co 2p spectra are recorded herein close to the previously reported values for Fe–N_x (*ca.* 710.5 eV) and Co–N_x (*ca.* 781.0 eV).[57,82,83] Among the oxidation states of +II and +III, the bivalent (+II) state is reported to provide the active TM site for the ORR in the M–N_x.[32,84] However, it should also be pointed out that the very close values and overlapping of the peaks +II/–N_x/+III create a somewhat similar situation in their specific distinction as the difficulty of peak separation is observed in N 1s spectra for pyridinic-N/M–N_x/pyrrolic-N (Fig. 5e). Still based on the XPS data collected herein, it would be safe to assume the verified existence of M–N_x, especially if the harsh acid treatment procedure within the fabrication process of the catalysts is considered (Section 2.1). In addition to individual Fe–N_x and Co–N_x sites, some of the M–N_x could be in the Co–Fe dual-atom configuration, which would be highly desirable for high ORR electrocatalytic activity.[26,30] Unfortunately, the XPS cannot unambiguously distinguish between single-atom and dual-atom M–N_x sites.

3.2. Half-cell oxygen reduction studies using RRDE and HT-GDE methods

The activity towards the ORR of the prepared M–N–C catalysts was first evaluated using the RRDE in a 0.5 M H_3PO_4 environment as it is known to be suitable for non-PGM cathode materials with HT-PEMFC target application.[78,85] According to one of the main aims of this investigation, the different nanocarbon

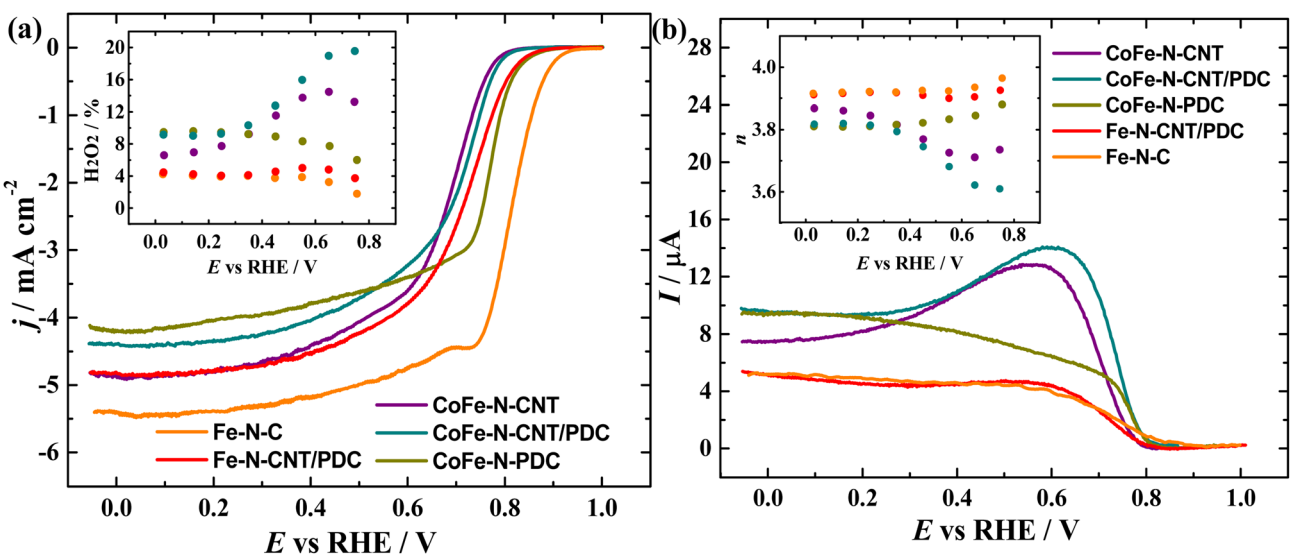


Fig. 6 Polarisation curves recorded with the RRDE method for (a) oxygen reduction at the disc and (b) H_2O_2 oxidation at the ring on different M–N–C coated GC-discs with a Pt-ring electrode in O_2-saturated 0.5 M H_3PO_4 at 1600 rpm and 10 mV s^{-1}. The insets show (a) peroxide yield (%) and (b) electron transfer number (*n*) as a function of potential.

 This journal is © The Royal Society of Chemistry 2026

Table 3 Oxygen reduction half-wave potential ($E_{1/2}$), current density at 0 V (j@0 V), mass activity values at 0.8 V (MA@0.80 V), average electron transfer number (n), and average peroxide yield (H_2O_2) obtained from RRDE voltammetry disc and ring curves at 1600 rpm in O_2-saturated 0.5 M H_3PO_4. All the values have been obtained from the iR-drop corrected I–E curves recorded with an M–N–C loading of 0.4 mg cm^{-2} shown in Fig. 6 and S6

Catalyst	$E_{1/2}$ (V *vs.* RHE)	j@0 V (mA cm^{-2})	MA@0.80 V (A g^{-1})	n	H_2O_2 (%)
CoFe–N–PDC	0.76	−4.2	2.4	3.8	8.6
CoFe–N–CNT/PDC	0.70	−4.4	0.4	3.7	13.1
CoFe–N–CNT	0.68	−4.9	0.2	3.8	10.4
Fe–N–CNT/PDC	0.71	−4.8	1.6	3.9	4.4
MnFe–N–CNT/PDC	0.70	−4.7	1.1	3.9	4.1
CoMnFe–N–CNT/PDC	0.71	−4.4	0.7	3.8	8.2
Fe–N–C	0.80	−5.4	16.0	3.9	3.6

backbone CoFe–N–C catalysts were first compared (Fig. 6a, b and Table 3). The half-wave potential ($E_{1/2}$) and current density at 0 V (j@0 V) values of CoFe–N–PDC are very similar to those of CoFe–N–SiOCa (0.4 mg cm^{-2}) from our previous investigation,[38] where Co and Fe salts were incorporated into the initial PDC precursor composition and not later during the ultrasonic mixing with ZIF-8. The addition of CNTs into the backbone leads to different effects. First, the j@0 V value increases with a higher proportion of CNTs, which is a beneficial observation for enhanced ORR activity. Simultaneously, a lower $E_{1/2}$ is observed, accompanied by a higher H_2O_2 yield between 0.3 and 0.8 V, which can be considered a negative effect on the ORR performance. For comparison, the Co-free derivative of CoFe–N–CNT/PDC was prepared to investigate the influence of Co inclusion (Fe–N–CNT/PDC). In 0.5 M H_3PO_4 solution at RT, there is no benefit of Co inclusion into the M–N–C composition for the ORR performance. This is an expected result as under these conditions Co–N_x sites are known to catalyse the ORR *via* the 2e$^-$ pathway, while Fe–N_x catalyse the 4e$^-$ route.[31,82] The mass activity value at 0.8 V (MA@0.80 V) of 1.6 A g^{-1} for Fe–N–CNT/PDC is in a similar range as the values reported for HNO_3-treated and carbon aerogel-based Fe–N–C in a parallel investigation by Zierdt *et al.*[78] Additionally, as the binary TM combination of Mn/Fe was found to be beneficial for obtaining low H_2O_2 yield in our previous study of PDC/ZIF-8 catalysts, the Mn-containing derivatives of CoFe–N–CNT/PDC and Fe–N–CNT/PDC were also prepared and investigated using the RRDE technique (Fig. S6a, b and Table 3). The inclusion of Mn decreased the H_2O_2 yield as expected, while having no noticeable effect on the $E_{1/2}$ and j@0 V values and finally decreasing the MA@0.80 V value compared to Fe–N–CNT/PDC. Under the RRDE conditions, the commercial Fe–N–C (PMF-011904, Pajarito Powder, LLC) outperformed all the M–N–C catalysts prepared herein, which is similar to our previous investigation of binary TM combination ZIF-8/PDC catalysts.[38] As a main reason, the higher ORR performance of Fe–N–C can be explained by the considerably higher SSA as determined in a recent study (S_{BET} = 597.7 m^2 g^{-1}).[38] Compared to the alternative bimetal M–N–C investigated using the RRDE in 0.5 M H_3PO_4 for HT-PEMFC target application, the recent ZIF-8 derived Fe–Sn–N–C (1 : 0.3) exhibiting a remarkable MA@0.80 V of 19.3 A g^{-1} should be outlined from a recent investigation by Buschermöhle *et al.*[48]

As the long-term stability of the M–N–C is one of the most important issues under HT-PEMFC conditions, the accelerated durability test (ADT) protocol of 24 hours in 0.5 M H_3PO_4 from our previous study[38] was implemented (Fig. S7). The smallest decline in the $E_{1/2}$ value after 10 000 CV cycles was observed for the CNT-free CoFe–N–PDC catalyst ($\Delta E_{1/2}$ = 21 mV), which is in good accordance with the older investigation (CoFe–N–SiOCa)[38] and refers to the PDC nanocarbon backbone's good durability. In the case of CNT/PDC-based materials, a higher $\Delta E_{1/2}$ of 54 is observed in the case of Fe–N–CNT/PDC compared to the $\Delta E_{1/2}$ of 48 for CoFe–N–CNT/PDC. This could indicate the scavenging of ROS due to the inclusion of Co–N_x or Fe/Co–N_x sites compared to the only Fe-containing M–N–C.[23,25] For the catalyst-coated RRDE disc areas, the SEM measurements and EDX analysis can also be performed before and after implementing the ADT (Fig. S8 and Table S3). SEM images show no visible differences before and after stability testing, whereas EDX analysis reveals some differences. For both studied CoFe–N–C samples, a similar decrease in the Fe and Co content is observed, most likely due to demetallation of M–N_x sites during the ADT. At the same time, the amount of Mo does not decrease, confirming that Mo is not at the center of the M–N_x sites on the catalyst surface, but is rather hidden inside the nanotubes and therefore inactive for the surface reactions. The new component F, which was not observed during the original physical characterisation of the M–N–C in Section 3.1, originates from the Nafion® binder.

Furthermore, the CV responses of the prepared M–N–C catalysts were recorded using a potential scan rate of 50 mV s^{-1} in Ar- and O_2-saturated 0.5 M H_3PO_4 (Fig. S9). The determined ORR peak potentials (E_p) follow the same general trend as that observed for the $E_{1/2}$ values for the RRDE measurements (Table 3). However, the highest E_p value of 0.69 V of CoFe–N–PDC outperforms the E_p = 0.65 V determined in the previous investigation for both CoFe–N–SiOCa and commercial Fe–N–C,[38] indicating that CoFe–N–PDC is a superior ORR electrocatalyst under these specific conditions of CV measurements. This is very likely an overevaluation as RRDE results are more reliable due to the benefits of hydrodynamic conditions, iR-drop correction, and the removal of the background current.

From the HT-PEMFC target application point of view, the ORR investigations in the HT-GDE are considerably closer to the real device conditions compared to the RRDE conditions at RT.

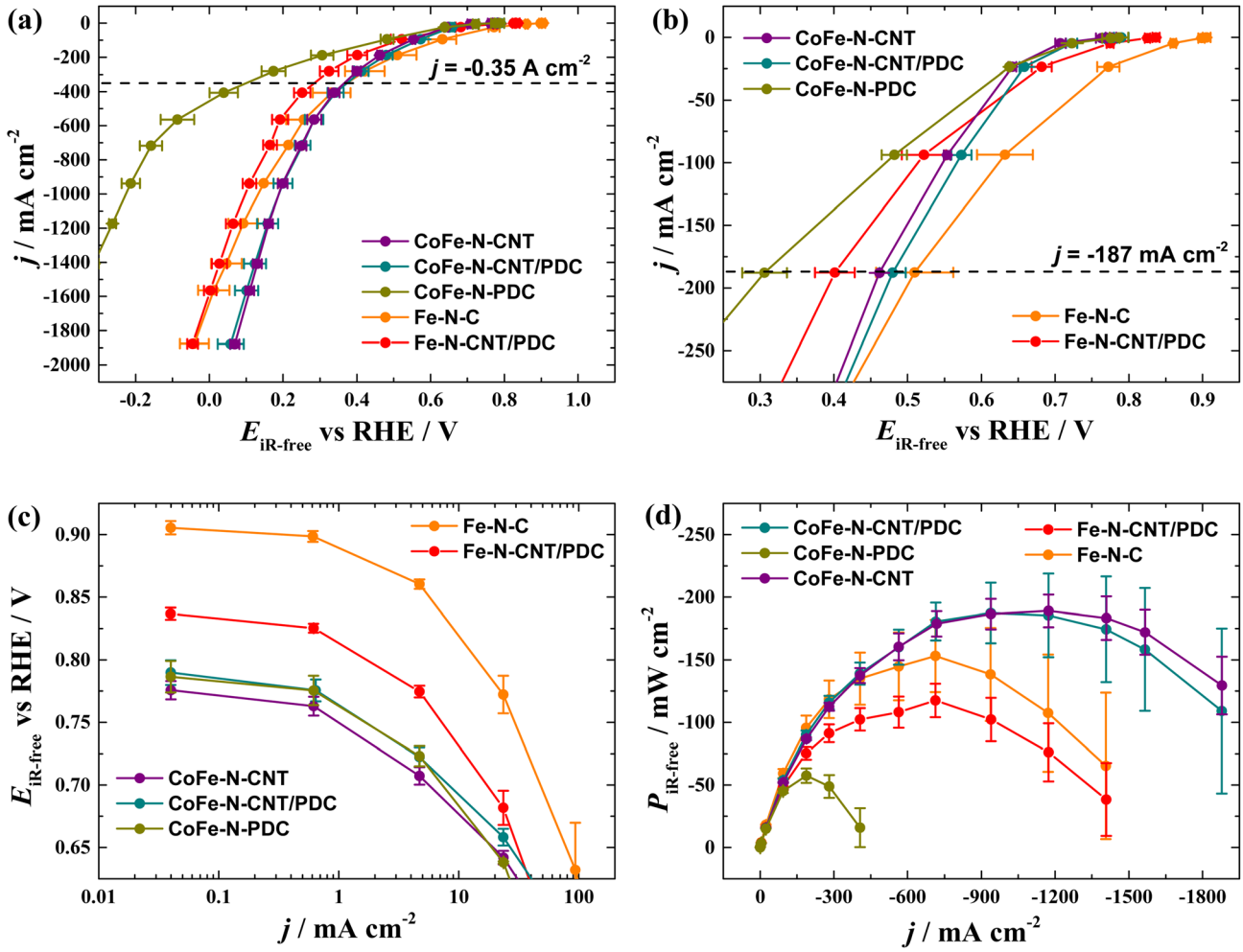


Fig. 7 (a and b) HT-GDE half-cell polarisation curves of M–N–C coated (4.2 mg cm^{-2}) GDEs for the ORR measured using an O_2 flow rate of 0.15 L min^{-1}, 160 °C, conc. H_3PO_4, and PA-PBI membrane. (c) Semi-logarithmic plots of the polarisation curves and (d) calculated power density curves.

Therefore, all the M–N–C prepared in this work and Fe–N–C for comparison were further evaluated using the HT-GDE setup as ORR catalysts (Fig. 7, S10 and Table 4). First, the HT-GDE setup modifications implemented in the present investigation were evaluated using the commercial Fe–N–C catalyst. In a previous study using a Cu current collector (CC) and a catalyst loading (CL) of 3.0 mg cm^{-2}, the open-circuit potential (OCP) and potential value at 187 mA cm^{-2} (E_{187}) were recorded as 865 ± 24 and 421 ± 27 mV, respectively.[38] Herein, considerably higher activity towards the ORR was observed for Fe–N–C with an OCP = 905 ± 5 and E_{187} = 510 ± 52 mV, which can be attributed to the use of a stainless steel CC and CL of 4.2 mg cm^{-2} (Section S3). In addition to the influence of higher CL, it is likely that Cu ions from the CC can poison the PA-PBI membrane as supported by corresponding information published for Nafion™ membranes in LT-PEMFC application.[86] According to the already discussed RRDE results, there was no observable difference in the ORR activity of the final catalysts if the Co and Fe salts are incorporated into the initial PDC precursor (CoFe–N–SiOCa)[38] or later during the ultrasonic mixing step (CoFe–N–PDC, this work). In the case of the HT-GDE setup, the situation is different as CoFe–N–SiOCa tested with the Cu CC and lower CL showed E_{187} = 360 ± 27 mV,[38] while only E_{187} = 306 ± 30 was recorded for CoFe–N–PDC herein. This considerable difference in the ORR performance between the RRDE and HT-GDE for otherwise identical catalysts may result from the large difference in temperature and electrolyte acid concentration, showing the superiority of HT-GDE testing if the HT-PEMFC is the target application. The inclusion of CNTs into the CoFe–N–C catalyst composition causes an increase in the ORR activity, which is so significant that CoFe–N–CNT/PDC outperforms Fe–N–C at potential values less than *ca.* 0.3 V. If the nanocarbon backbone consists only of CNTs without any PDC, then the ORR performance decreases in the potential range relevant for real-life fuel cell applications (higher than *ca.* 0.5 V, Fig. 7b and c).[2] The collected HT-GDE data indicate that the CNT/PDC composite could be a more suitable backbone for HT-PEMFC cathode M–N–C material development than PDC or CNTs alone. To assess the benefit of Co in CoFe–N–CNT/PDC composition, the HT-GDE curve of Fe–N–CNT/PDC can be

 This journal is © The Royal Society of Chemistry 2026

Table 4 HT-GDE half-cell testing results, open circuit potential (OCP), potential value at 187 mA cm^{-2} (E_{187}), and maximum power density (P_{max}) normalised to the surface area and M–N–C weight using the M–N–C loading (4.2 mg cm^{-2}) for the ORR derived from the HT-GDE polarisation curves with different M–N–C catalysts shown in Fig. 7 and S10

Catalyst	OCP (mV *vs.* RHE)	E_{187} (mV *vs.* RHE)	P_{max} (mW cm^{-2})	P_{max} (W $g_{Catalyst}^{-1}$)
Fe–N–C	905 ± 5	510 ± 52	153 ± 29	36 ± 7
Fe–N–CNT/PDC	837 ± 5	401 ± 27	117 ± 13	28 ± 3
MnFe–N–CNT/PDC	813 ± 2	337 ± 27	77 ± 14	18 ± 3
CoMnFe–N–CNT/PDC	808 ± 1	404 ± 17	112 ± 10	27 ± 2
CoFe–N–CNT/PDC	790 ± 10	480 ± 18	187 ± 24	45 ± 6
CoFe–N–CNT	776 ± 7	462 ± 7	189 ± 13	45 ± 3
CoFe–N–PDC	786 ± 13	306 ± 30	57 ± 6	14 ± 1

studied. The commercial Fe–N–C outperforms Fe–N–CNT/PDC throughout the ORR polarisation curve, while the superiority of Fe–N–CNT/PDC over CoFe–N–CNT/PDC is observed in the low polarisation current region between 0 and −50 mA cm^{-2} (Fig. 7b and c). The latter is in accordance with the RRDE results as this method operates under similar low j conditions if a 10× difference in the CL value is considered (Fig. 6). Furthermore, in the case of Mn-containing catalysts, the RRDE and HT-GDE results follow the very same trend with Fe–N–CNT/PDC supremacy (Fig. S10 and Table 4). In the higher polarisation current region, the superiority of CoFe–N–CNT(/PDC) over other M–N–C catalysts is clearly observed in the case of calculated power density curves (Fig. 7d). The maximum power density (P_{max}) of Fe–N–C is obtained at *ca.* 153 mW cm^{-2}, which is in good accordance with the previous HT-GDE investigations with the ultrasonic spray-coated Fe–N–C catalyst exhibiting 142 mW cm^{-2}.[87] In the case of CoFe–N–CNT(/PDC), a P_{max} of *ca.* 188 mW cm^{-2} is obtained (Table 4), which indicates that these catalysts are the most suitable for the application at the HT-PEMFC cathode in this work.

The trend of ORR activity is similar among CoFe–N–CNT(/PDC) and Fe–N–C catalysts between RRDE (Fig. 6a) and HT-GDE setups within a polarisation current density range from 0 to −0.35 A cm^{-2} (Fig. 7a). Between −0.35 and 1.9 A cm^{-2}, the superior ORR performance of CoFe–N–CNT(/PDC) over Fe–N–C could be due to the change in deactivation mechanisms of M–N–C cathodes during PEMFC operation at HT influencing the M–N–C stability compared to the RRDE experiments at RT according to the investigation by Bae *et al.*[88] Also, the synergistic effect between Fe–N_x and Co–N_x or Fe/Co–N_x could be amplified due to the HT conditions improving the activity towards the ORR. The CVs recorded before and after the measurements for HT-GDE half-cell polarisation curves are shown in Fig. S11 for Fe–N–C and CoFe–N–CNT/PDC. In this work, the CVs recorded before and after are considerably more similar, indicating that the GDE system is less influenced by the tests compared to the previous investigation.[38] This difference could be favoured by the higher CL and stainless steel CC used in the present study. The lower capacitive current under the CV of CoFe–N–CNT/PDC compared to that of Fe–N–C is consistent with the higher SSA of the latter catalyst.

One of the major issues for M–N–C catalysts in HT-PEMFCs is the stability due to the harsh conditions, and the ADT protocol used for 0.5 M H_3PO_4 solution, including RRDE and 10 000 CV experiments (Fig. S7), could underestimate the M–N–C stability due to the lower temperature and lower acid concentration.[13,23,43] Therefore, the stability testing procedure in the HT-GDE setup was implemented for the very first time using chronopotentiometry with a constant current value of 0.1 A cm^{-2} from earlier Fe–N–C stability investigations at the HT-PEMFC cathode.[23] The testing was carried out over 3 hours with EIS measurement after every 20 minutes to include the iR-drop correction data throughout the measurement (Fig. 8). As expected, the obtained results indicate the observable decline in the ORR performance of M–N–C, similar to the case of the ADT protocol used in 0.5 M H_3PO_4. Fe–N–C exhibited the highest ORR voltage loss of 80 mV over the experiment, while still being the most active catalyst after the testing, with final $E_{iR\text{-}free}$ = 0.51 V. All other M–N–C materials exhibited a voltage loss between 30–60 mV, with the highest final $E_{iR\text{-}free}$ of 0.48 and 0.46 V for CoFe–N–CNT/PDC and CoFe–N–CNTs, respectively. On the other hand, when both CNT-containing CoFe–N–C catalysts showed a similar voltage loss of *ca.* 60 mV, CoFe–N–PDC showed only 36 mV (Fig. 8b). This situation is similar to the lowest $\Delta E_{1/2}$ value observed for CoFe–N–PDC after ADT in 0.5 M H_3PO_4 solution among different CoFe–N–C catalysts (Fig. S7). In conclusion, the superior durability of PDC over CNTs in the M–N–C backbone was verified under both durability testing conditions, using the RRDE technique at RT (24 h) and the HT-GDE half-cell at 160 °C (3 h). The considerably higher voltage loss of Fe–N–CNT/PDC (60 mV) compared to the lowest registered voltage loss for CoMnFe–N–CNT/PDC (30 mV) in Fig. 8a can indicate that Co–N_x and Mn–N_x could help prevent the formation of or scavenge ROS from Fe–N_x sites under HT conditions, but proving this would require further experimental verification. The short 3-hour period for the stability test is due to the HT-GDE setup's operating limitations, while it still describes the most rapid ORR activity loss region of M–N–C according to published HT-PEMFC results.[23,88]

When the CVs recorded before and after the 3-hour test are compared, the appearance of redox peaks at *ca.* 0.25 and 0.5 V is observed in the case of multiple metal co-doped M–N–C compared to Fe–N–C and Fe–N–CNT/PDC catalysts (Fig. S12 and S13). Both responses could correspond to the electrochemical transitions in TM (alloy) nanoparticles (*e.g.* Fe^{2+}/Fe^{3+}), which were observed during the HR-TEM experiments (Fig. 4 and S2,

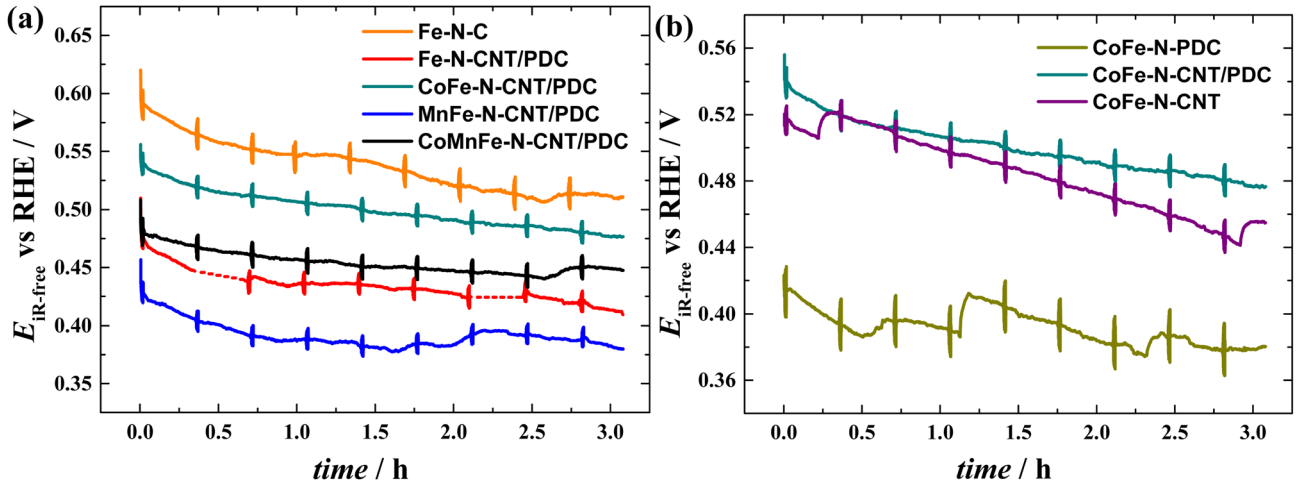


Fig. 8 Chronopotentiometry measurements at 0.1 A cm^{-2} using the HT-GDE half-cell setup with different (a) M–N–C and (b) CoFe–N–C coated (4.2 mg cm^{-2}) GDEs for the ORR measured using an O_2 flow rate of 0.15 L min^{-1}, 160 °C, conc. H_3PO_4, and a PA-PBI membrane. EIS measurements were performed after every 20 minutes.

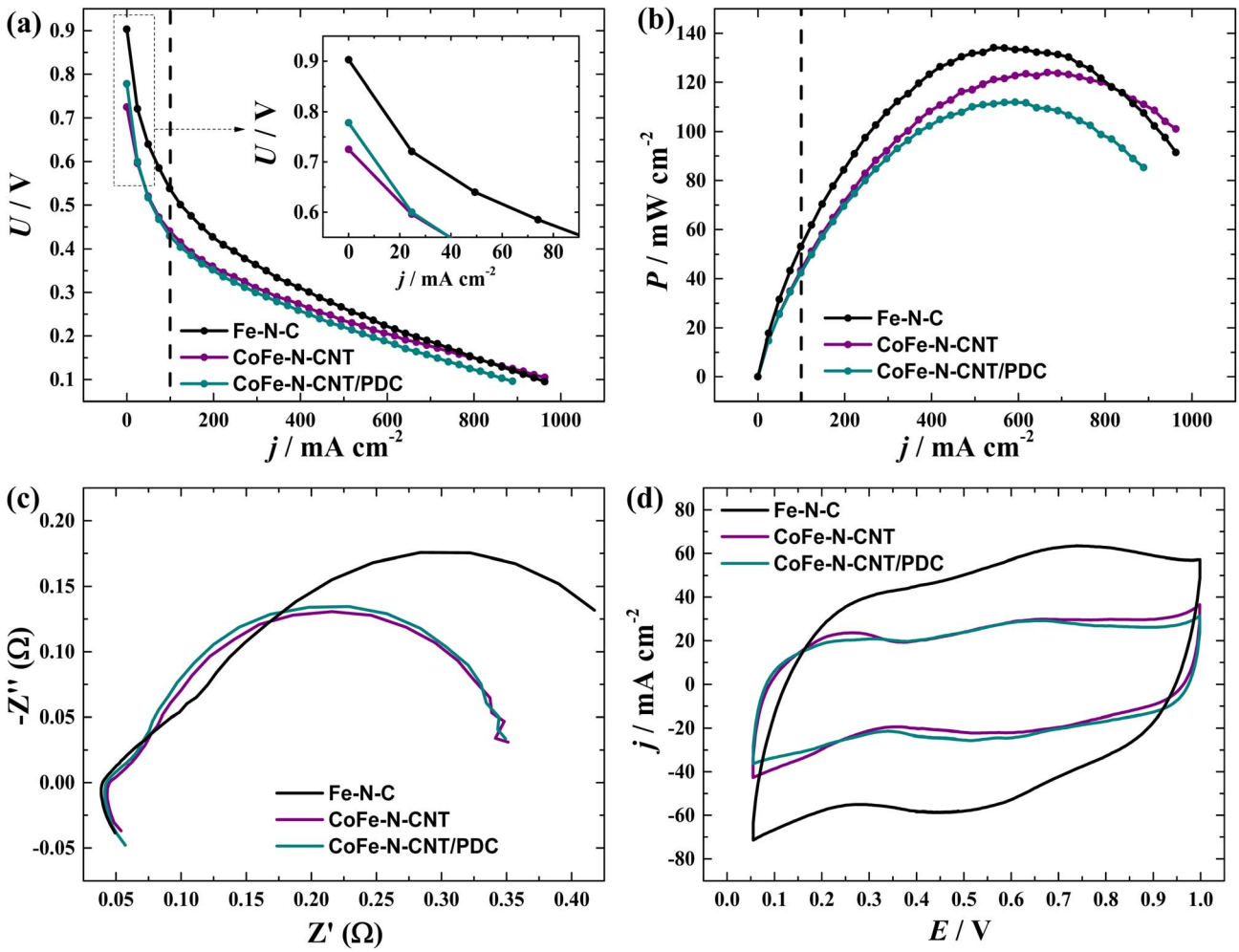


Fig. 9 HT-PEMFC measurements with M–N–C cathode catalysts (3.5 mg cm^{-2}), (a) galvanostatic polarisation curves and (b) calculated power density curves recorded under H_2/O_2 (1.5/9.5) at 160 °C, (c) Nyquist plots from EIS at 0.1 A cm^{-2} recorded with dry H_2/O_2 (1.5/9.5), and (d) CVs recorded under a H_2/N_2 flow rate of 0.1 L min^{-1} and scan rate of 100 mV s^{-1}.

This journal is © The Royal Society of Chemistry 2026

Table 5 HT-PEMFC testing results with various M–N–C cathodes performed in this investigation and from the previous literature reports, open-circuit voltage (OCV), power density at 100 mA cm^{-2} (P_{100}), maximum power density (P_{max}), and cell temperature (T). All results are reported for the PA-PBI membrane and Pt/C anode catalyst-based MEAs operated with dry O_2/H_2 gases

Cathode catalyst	OCV (V)	M–N–C loading (mg cm^{-2})	P_{100} (mW cm^{-2})	P_{max} (mW cm^{-2})	T (°C)	Ref.
Fe–N–C	0.90	3.5	62	134	160	This work
CoFe–N–CNT/PDC	0.78	3.5	42	112	160	This work
CoFe–N–CNT	0.73	3.5	43	124	160	This work
CoFe–N–SiOCa	0.77	3.0	34	50	160	38
Co–N/MWCNT	0.96[b]	3.0	52[a,b]	66[b]	160	70
Fe–Sn–N–C	0.86	3.1	35	53	160	48
Fe–N-ox-BP	0.82	3.1	39	67	160	23
FeCu(4 : 1)	—	4.0	68[a]	250	160	91
FeCu(4 : 1)	0.88	4.0	75[a]	302	230	91

[a] Values determined from the figures provided in the paper. [b] Experiment performed with dry air fed to the cathode instead of O_2 gas.

S3).[78,89,90] However, the redox response at 0.5 V can also include the hydroquinone/quinone (HQ/Q) species introduced due to the carbon corrosion.[23,29,87] The 3-hour operating data show that CoFe–N–CNT(/PDC) and Fe–N–C could be the most promising catalysts for the HT-PEMFC cathode among the M–N–C catalysts studied herein.

3.3. HT-PEMFC testing

Single-cell tests were conducted with the three pre-selected (Section 3.2) cathode catalysts (CoFe–N–CNT(/PDC) and Fe–N–C), the PA-PBI membrane, and a commercial Pt/C anode. In this work, the M–N–C catalysts were drop-cast onto the cathode GDL resulting in a CL of 3.5 mg cm^{-2}. The data obtained for HT-PEMFC tests are shown in Fig. 9 and Table 5. Firstly, the results for commercial Fe–N–C (P_{100} = 62 mW cm^{-2}; P_{max} = 134 mW cm^{-2}) are in accordance with the previous data (CL = 3.1–3.5 mg cm^{-2}, P_{100} = 53–56 mW cm^{-2}, and P_{max} = 140–155 mW cm^{-2}) reported for ultrasonically coated and doctor-bladed Fe–N–C cathodes investigated in HT-PEMFCs in an earlier investigation.[90] Both CoFe–N–C catalysts exhibit lower HT-PEMFC current density than Fe–N–C, especially at 0.65–0.7 V and up near the activation polarisation region, whose voltages are important for LDV and HDV application points of view.[2] This observation is in accordance with the HT-GDE results, where Fe–N–C outperformed CoFe–N–C in the low polarisation current density range (−0.35 to 0 A cm^{-2}, Fig. 7). The observed difference in the higher polarisation current density region, where compared to HT-GDE tests, Fe–N–C is still more active than both CoFe–N–C catalysts, could be due to the different acid wetting conditions of the PA-PBI membrane in these devices and a 20% higher amount of catalyst at the HT-GDE cathode. The overall superior HT-PEMFC performance of Fe–N–C over CoFe–N–CNT(/PDC) can be first attributed to its higher OCV value, likely due to the higher intrinsic activity and better accessibility of the Fe–N_x sites in Fe–N–C. Secondly, the lowest ohmic resistance for Fe–N–C (Fig. 9c) indicates a better electrical conductivity and/or more successful integration with the PA-PBI membrane in the case of Fe–N–C. Thirdly, similarly to the HT-GDE tests (Fig. S11–S13), the highest surface area under the CV curve (Fig. 9d) is also observed in the case of Fe–N–C, which is supported by the considerably higher S_{BET} value (597.7 m^2 g^{-1})[38] compared to CoFe–N–CNT(/PDC) (Table 1). Also, the lower area under the CV curve for CoFe–N–CNT(/PDC) could indicate a lower acid coverage, leading to fewer accessible active sites than in Fe–N–C. Between CoFe–N–C catalysts, the CoFe–N–CNTs shows superior performance at j values more than 100 mA cm^{-2} and CoFe–N–CNT/PDC shows between j = 0 and *ca.* 25 mA cm^{-2}. The latter region of low j is more important from a practical application point of view as this region corresponds to 0.6–0.8 V.[2]

There is no prior knowledge of any CoFe–N–C application at the HT-PEMFC cathode besides our own previous work, where CoFe–N–SiOCa with only a PDC-based backbone[38] showed inferior performance compared to both CoFe–N–CNT(/PDC) tested herein (Table 5). The incorporation of Co into the M–N–C catalyst composition for HT-PEMFC is strongly supported by a study by Eren *et al.*,[70] where the Co–N/MWCNT cathode fed with dry air showed a remarkable P_{100} of 52 mW cm^{-2}. Among bimetallic M–N–C catalysts, the state-of-the-art at 160 °C operation is currently the FeCu(4 : 1) catalyst by Cheng *et al.*,[91] reported with a P_{100} and P_{max} of 68 and 250 mW cm^{-2}, respectively, under the HT-PEMFC conditions with an improved SiO_2-doped PA/PBI composite membrane. Nevertheless, the novel CoFe–N–CNT/PDC catalyst prepared herein for the HT-PEMFC cathode outperforms several previously developed bimetallic M–N–C catalysts (Table 5).

4. Conclusions

In the present investigation, a double TM- and N-functionalised M–N–C catalyst with an optimised nanocarbon backbone was developed for the HT-PEMFC cathode. The preliminary testing of different M–N–C materials towards the ORR activity was performed comparably using the RRDE technique at RT and using an HT-GDE half-cell at 160 °C. The RRDE tests in 0.5 M H_3PO_4 solution showed the superiority of PDC as a single backbone component catalyst (CoFe–N–PDC) according to the $E_{1/2}$ value of 0.76 V *vs.* RHE and MA@0.80 V of 2.4 A g^{-1}. Under the HT-GDE conditions, CoFe–N–CNT/PDC and CoFe–N–CNTs showed remarkable ORR activity by outperforming even the

commercial Fe–N–C in the $j = -0.35$ to -1.9 A cm^{-2} range. P_{max} values of around 188 mW cm^{-2} were obtained with both CoFe–N–CNT(/PDC) catalysts compared to Fe–N–C (153 mW cm^{-2}) under HT-GDE conditions. The 3-hour durability test at a constant current density of 100 mA cm^{-2} in the HT-GDE showed an ORR voltage loss of 80 mV for Fe–N–C, while the corresponding value for CoFe–N–CNT/PDC and CoFe–N–CNTs was *ca.* 60 mV. The superior durability of PDC as the M–N–C backbone component was observed under two different types of durability testing conditions, using the RRDE technique with 10 000 CV cycles (CoFe–N–PDC, $\Delta E_{1/2} = 21$ mV) and the HT-GDE half-cell 3-hour test at 100 mA cm^{-2} (CoFe–N–PDC, voltage loss = 36 mV). One of the reasons for the decrease in ORR activity of CoFe–N–C catalysts was found to be demetallation of M–N_x sites, which was confirmed by EDX analysis before and after the ADT under RRDE conditions. On the other hand, HT-GDE tests indicated that the inclusion of Co and Mn into the M–N–C catalyst could help scavenge or reduce the ROS production at Fe–N_x sites. During application at the HT-PEMFC cathode, the overall superiority of Fe–N–C was witnessed (P_{max} = 134 mW cm^{-2}), while the corresponding values for CoFe–N–C reached 83–93% of those of Fe–N–C. In the voltage range relevant to LDV and HDV applications, CoFe–N–CNT/PDC outperformed CoFe–N–CNTs. The high activity towards the ORR of the prepared catalysts was mainly attributed to the presence of Fe-, Co-, and N-based active sites (*e.g.* Co–N_x, Fe–N_x, pyridinic-N, and graphitic-N) detected in the nanocarbon matrix and TM (alloy) NPs by XPS and TEM techniques. The inclusion of CNTs together with PDC into the nanocarbon backbone of M–N–C increased the SSA, enabling the fabrication of an optimal CoFe–N–CNT/PDC catalyst for HT-PEMFC application.

Conflicts of interest

There are no conflicts to declare.

Data availability

The data supporting this study are available at the following repository. See DOI: https://doi.org/10.23673/re-576.

Supplementary information (SI) is available. See DOI: https://doi.org/10.1039/d6ta01012a.

Acknowledgements

This study was financially supported by the Estonian Research Council grant (PUTJD1170). M. M. acknowledges DLR and the German Academic Exchange Service (DAAD) for the funding *via* DLR-DAAD Research Fellowship No. 521. The XPS instrument was funded by the German Research Foundation (DFG) through grant INST 184/144–1 FUGG. The authors acknowledge the Electron and Light Microscopy Service Unit of the School of Mathematics and Science of the Carl von Ossietzky University for the use of the imaging facilities. The authors acknowledge the opportunity to conduct Raman measurements at the University of Oldenburg in the working group of Christian Schneider, with assistance from Nico Ruskaup. This research was also supported by the Estonian Ministry of Education and Research (TK210, Centre of Excellence in Sustainable Green Hydrogen and Energy Technologies). We would like to thank the following experts at the University of Tartu, Jaan Aruväli for conducting the XRD analyses, Marian Külaviir and Dr Peeter Paaver for performing the ICP-MS analyses, and Dr Vambola Kisand and Markus Otsus for performing SEM-EDX measurements.

References

1 E. Eikeng, A. Makhsoos and B. Pollet, *Int. J. Hydrog. Energy*, 2024, **71**, 433–464.
2 G. Yang, C. Lee, X. Qiao, S. Babu, U. Martinez and J. Spendelow, *Electrochem. Energy Rev.*, 2024, **7**, 9.
3 S. Kazula, S. de Graaf and L. Enghardt, *J. Glob. Power Propuls. Soc.*, 2023, **7**, 43–57.
4 D. Gopalasingam, B. Rakhshani and C. Rodriguez, *Hydrogen*, 2025, **6**, 92.
5 F. Franke, A. Link and S. Kazula, *CEAS Aeronaut. J.*, 2025, DOI: 10.1007/s13272-025-00908-0.
6 A. Zucconi, J. Hack, R. Stocker, T. A. M. Suter, A. J. E. Rettie and D. J. L. Brett, *J. Mater. Chem. A*, 2024, **12**, 8014–8064.
7 A. Belmesov, L. Shmygleva, A. Baranov and A. Levchenko, *Russ. Chem. Rev.*, 2024, **93**, RCR5121.
8 W. Li, X. Luo, Y. Zhou, J. Shen, Y. Chen, Y. Liu and J. Qiao, *Process Saf. Environ. Protect.*, 2025, **199**, 113837.
9 F. Kourougianni, A. Arsalis, A. Olympios, G. Yiasoumas, C. Konstantinou, P. Papanastasiou and G. Georghiou, *Renewable Energy*, 2024, **231**, 120911.
10 Z. Xia, X. Zhang, X. Xu, J. Huang, C. Zhuang, J. Wang, S. Yu, S. Wang and G. Sun, *Appl. Catal., B*, 2025, **371**, 125282.
11 S. Choi, I. Jang and S. Lee, *Crystals*, 2025, **15**, 129.
12 L. Gong, L. Tao, L. Wang, X. Fu and S. Wang, *Chin. J. Catal.*, 2025, **68**, 155–176.
13 N. Narayanan, B. Ravichandran, I. Emayavaramban, H. Liu and H. Su, *Catalysts*, 2025, **15**, 775.
14 J. M. Linge, X. Lyu, H. Yu, H. Meyer III, M. Lehmann, T. Saito, D. Cullen and A. Serov, *Johns. Matthey Technol. Rev.*, 2025, **70**, e70302.
15 J. Wang, B. Liu, X. Wang, S. Lu, Y. Xiang and J. Zhang, *J. Power Sources*, 2025, **645**, 237178.
16 J. Müller-Hülstede, L. Uhlig, H. Schmies, D. Schonvogel, Q. Meyer, Y. Nie, C. Zhao, J. Vidakovic and P. Wagner, *ChemSusChem*, 2023, **16**, e202202046.
17 I. Sebbani, M. Ettouhami and M. Boulakhbar, *Clean. Energy Syst.*, 2025, **10**, 100168.
18 N. Seselj, S. M. Alfaro, E. Bompolaki, L. N. Cleemann, T. Torres and K. Azizi, *Adv. Mater.*, 2023, **35**, 2302207.
19 Q. Meyer, C. J. Yang, Y. Cheng and C. Zhao, *Electrochem. Energy Rev.*, 2023, **6**, 16.
20 C. Yue, W. Zheng, Q. Wang, Z. Wang, B. Li, C. Zhang and P. Ming, *Energy Environ. Sci.*, 2025, **18**, 6934–6982.
21 Y. Liu, R. Li, J. Xia, C. Shu, J. Liu, S. Yan, R. Jin, H. Chen, L. Teng, Y. Si, C. Guo, Y. Zhang and Q. Xu, *Nano Res.*, 2025, **18**, 94907244.

 This journal is © The Royal Society of Chemistry 2026

22 X. Xie, B. Li, P. Xu, M. Sougrati, R. Garcia-Serres, D. Cullen, A. Kropf, F. Xia, M. Song, S. Saha, Y. Zeng, M. Engelhard, M. Bowden, H. Zhang, L. Yan, T. Lemmon, X. Li, U. Martinez, Y. Cheng, G. Wu, P. Zelenay, V. Ramani, D. Myers, F. Jaouen, L. Yang, G. Wang and Y. Shao, *J. Am. Chem. Soc.*, 2025, **147**, 48117–48126.

23 J. Müller-Hülstede, H. Schmies, D. Schonvogel, Q. Meyer, Y. Nie, C. Zhao, P. Wagner and M. Wark, *Int. J. Hydrog. Energy*, 2024, **50**, 921–930.

24 Q. Meyer, Y. Nie, M. R. Bin Mamtaz and C. Zhao, *ACS Electrochem.*, 2025, **1**, 1206–1230.

25 K. Kumar, L. Dubau, F. Jaouen and F. Maillard, *Chem. Rev.*, 2023, **123**, 9265–9326.

26 M. Moghaddam, M. Kafshgari, A. Bahari, L. Kafshgari and A. Jafari, *J. Energy Chem.*, 2025, **107**, 305–344.

27 X. Zhao, Z. Hao, X. Zhang, L. Li, Y. Gao and L. Liu, *Chem. Eng. J.*, 2024, **497**, 155005.

28 K. Jannath and H. Saputra, *Electrochem. Sci. Adv.*, 2025, **5**, e202400033.

29 M. Gollasch, J. Müller-Hülstede, H. Schmies, D. Schonvogel, P. Wagner, A. Dyck and M. Wark, *Catalysts*, 2021, **11**, 841.

30 B. Wang, T. Zhang, G. Wang, X. Han, X. Zheng, G. Mao and Q. Wang, *Sep. Purif. Technol.*, 2025, **356**, 129934.

31 L. C. P. Pérez, N. R. Sahraie, J. Melke, P. Elsässer, D. Teschner, X. Huang, R. Kraehnert, R. J. White, S. Enthaler, P. Strasser and A. Fischer, *Adv. Funct. Mater.*, 2018, **28**, 1707551.

32 Z. Jiang, X. R. Liu, X. Z. Liu, S. Huang, Y. Liu, Z. C. Yao, Y. Zhang, Q. H. Zhang, L. Gu, L. R. Zheng, L. Li, J. A. Zhang, Y. J. Fan, T. Tang, Z. B. Zhuang and J. S. Hu, *Nat. Commun.*, 2023, **14**, 1822.

33 F. Luo, S. Wagner, W. Ju, M. Primbs, S. Li, H. Wang, U. I. Kramm and P. Strasser, *J. Am. Chem. Soc.*, 2022, **144**, 13487–13498.

34 T. Sun, B. B. Tian, J. Lu and C. L. Su, *J. Mater. Chem. A*, 2017, **5**, 18933–18950.

35 J. Piir, J. Lilloja, M. Käärik, J. Kozlova, A. Kikas, A. Treshchalov, J. Aruväli, V. Kisand, J. Leis, K. Kukli and K. Tammeveski, *Electrochim. Acta*, 2025, **527**, 146226.

36 J. Lilloja, E. Kibena-Põldsepp, A. Sarapuu, J. C. Douglin, M. Käärik, J. Kozlova, P. Paiste, A. Kikas, J. Aruväli, J. Leis, V. Sammelselg, D. R. Dekel and K. Tammeveski, *ACS Catal.*, 2021, **11**, 1920–1931.

37 J. Lilloja, E. Kibena-Põldsepp, A. Sarapuu, A. Konovalova, M. Käärik, J. Kozlova, P. Paiste, A. Kikas, A. Treshchalov, J. Aruväli, A. Zitolo, J. Leis, A. Tamm, V. Kisand, S. Holdcroft and K. Tammeveski, *ACS Appl. Energ. Mater.*, 2023, **6**, 5519–5529.

38 M. Mooste, J. Müller-Hülstede, D. Schonvogel, T. Zierdt, J. Buschermöhle, K. Fuhrmann, M. Wilhelm, P. Wagner and K. A. Friedrich, *Electrochim. Acta*, 2025, **514**, 145620.

39 M. Mooste, R. Kumar, S. Juvanen, J. Kozlova, A. Kikas, A. Treshchalov, M. Käärik, J. Aruväli, J. Leis, V. Kisand, K. Kukli, D. Schonvogel, P. Wagner, M. Wilhelm, K. Tammeveski and K. A. Friedrich, *Int. J. Energy Res.*, 2025, **2025**, 4252866.

40 P. Moni, M. G. Pollachini, M. Wilhelm, J. Lorenz, C. Harms, M. M. Murshed and K. Rezwan, *ACS Appl. Energ. Mater.*, 2019, **2**, 6078–6086.

41 P. Moni, M. Mooste, K. Tammeveski, K. Rezwan and M. Wilhelm, *RSC Adv.*, 2021, **11**, 39707–39717.

42 S. Abinaya, P. Moni, V. Parthiban, A. K. Sahu and M. Wilhelm, *ChemElectroChem*, 2019, **6**, 3268–3278.

43 X. Wu, S. Xing, J. Luo, H. Wang, F. Huang and C. Zhao, *Energy Rev.*, 2025, **4**, 100130.

44 D. Schonvogel, J. Hülstede, P. Wagner, I. Kruusenberg, K. Tammeveski, A. Dyck, C. Agert and M. Wark, *J. Electrochem. Soc.*, 2017, **164**, F995–F1004.

45 J. Yang, P. Ganesan, A. Ishihara and N. Nakashima, *ChemCatChem*, 2019, **11**, 5929–5944.

46 J. Müller-Hülstede, D. Schonvogel, H. Schmies, P. Wagner, A. Dyck and M. Wark, *ACS Appl. Energy Mater.*, 2021, **4**, 6912–6922.

47 J. Hülstede, D. Schonvogel, H. Schmies, P. Wagner, F. Schröter, A. Dyck and M. Wark, *Materials*, 2021, **14**, 45.

48 J. G. Buschermöhle, J. Müller-Hülstede, H. Schmies, D. Schonvogel, T. Zierdt, R. Lucka, F. Renz, P. Wagner and M. Wark, *ACS Catal.*, 2025, **15**, 4477–4488.

49 A. Dobrzanska-Danikiewicz, W. Wolany, D. Lukowiec, K. Jurkiewicz and P. Niedzialkowski, *Nanomater. Nanotechnol.*, 2017, **7**, 1847980417707173.

50 V. Eswaraiah, V. Sankaranarayanan and S. Ramaprabhu, *Nanoscale Res. Lett.*, 2011, **6**, 137.

51 Z. Li, L. Deng, I. Kinloch and R. Young, *Prog. Mater. Sci.*, 2023, **135**, 101089.

52 L. Ma, R. Wang, Y. H. Li, X. F. Liu, Q. Q. Zhang, X. Y. Dong and S. Q. Zang, *J. Mater. Chem. A*, 2018, **6**, 24071–24077.

53 W. J. Fan, Z. L. Li, C. H. You, X. Zong, X. L. Tian, S. Miao, T. Shu, C. Li and S. J. Liao, *Nano Energy*, 2017, **37**, 187–194.

54 H. Nguyen, J. Lee, E. Kwon, G. Lisak, B. Thanh, F. Ghanbari and K. Lin, *Chemosphere*, 2021, **279**, 130569.

55 D. Sayfiddinov, R. Kumar, V. Sakthivel, A. Kim, S. Kim, J. Hyun and D. Yoo, *ACS Mater. Lett.*, 2026, **8**, 161–170.

56 D. Sayfiddinov, R. Kumar, V. Sakthivel, S. Tamilarasi, A. Kim and D. Yoo, *J. Power Sources*, 2025, **652**, 237595.

57 R. Zhang, W. Guo, M. Wu, Z. Meng and H. Tang, *Energy Fuels*, 2025, **39**, 5956–5964.

58 A. Sokka, M. Mooste, M. Käärik, V. Gudkova, J. Kozlova, A. Kikas, V. Kisand, A. Treshchalov, A. Tamm, P. Paiste, J. Aruväli, J. Leis, A. Krumme, S. Holdcroft, S. Cavaliere, F. Jaouen and K. Tammeveski, *Int. J. Hydrog. Energy*, 2021, **46**, 31275–31287.

59 C. L. Li, M. C. Wu and R. Liu, *Appl. Catal., B*, 2019, **244**, 150–158.

60 S. Tian, S. Wu, J. Yang, J. Li, C. Liu, J. Shi, X. Xiang, L. Wang, Y. Sun and Q. Yang, *J. Electroanal. Chem.*, 2025, **980**, 118991.

61 H. Zhong, J. Wang, Y. Zhang, W. Xu, W. Xing, D. Xu, Y. Zhang and X. Zhang, *Angew. Chem., Int. Ed.*, 2014, **53**, 14235–14239.

62 Q. Wang, T. Ina, W. Chen, L. Shang, F. Sun, S. Wei, D. Sun-Waterhouse, S. Telfer, T. Zhang and G. Waterhouse, *Sci. Bull.*, 2020, **65**, 1743–1751.

63 A. Racz and M. Menyhard, *Appl. Surf. Sci. Adv.*, 2025, **30**, 100872.

64 J. C. Lascovich, R. Giorgi and S. Scaglione, *Appl. Surf. Sci.*, 1991, **47**, 17–21.
65 S. Turgeon and R. W. Paynter, *Thin Solid Films*, 2001, **394**, 43–47.
66 T. Canuto de Almeida e Silva, M. Mooste, E. Kibena-Põldsepp, L. Matisen, M. Merisalu, M. Kook, V. Sammelselg, K. Tammeveski, M. Wilhelm and K. Rezwan, *Catal. Sci. Technol.*, 2019, **9**, 854–866.
67 R. Kumar, M. Mooste, I. Zekker, M. Käärik, J. Leis, A. Kikas, A. Treshchalov, J. Kozlova, M. Otsus, J. Aruväli, V. Kisand, K. Kukli and K. Tammeveski, *Int. J. Hydrog. Energy*, 2025, **98**, 793–806.
68 X. Zhang, S. Wang, Z. Sun, Z. Ma, H. Wang, Z. Yang, Q. Chang and W. Chen, *Nano Res.*, 2025, **18**, 94907235.
69 R. Kumar, M. Mooste, Z. Ahmed, I. Zekker, M. Käärik, M. Marandi, J. Leis, A. Kikas, M. Otsus, A. Treshchalov, J. Aruväli, M. Jaagura, V. Kisand, A. Tamm and K. Tammeveski, *J. Environ. Chem. Eng.*, 2024, **12**, 112242.
70 E. Eren, N. Özkan and Y. Devrim, *Int. J. Hydrog. Energy*, 2020, **45**, 33957–33967.
71 Y. Jing, Y. Cheng, L. Wang, Y. Liu, B. Yu and C. Yang, *Chem. Eng. J.*, 2020, **397**, 125539.
72 M. Mooste, Z. Ahmed, P. Kapitulskis, R. Ivanov, A. Treshchalov, H.-M. Piirsoo, A. Kikas, V. Kisand, K. Kukli, I. Hussainova and K. Tammeveski, *Appl. Surf. Sci.*, 2024, **660**, 160024.
73 L. Li, N. Li, J. Xia, S. Zhou, X. Qian, F. Yin, G. He and H. Chen, *J. Mater. Chem. A*, 2023, **11**, 2291–2301.
74 J. Lee and W. Jung, *Mol. Catal.*, 2025, **580**, 115107.
75 S. Dongre, G. Zuccante, M. Muhyuddin, C. Vecchio, V. Baglio, E. Berretti, A. Lavacchi, R. Shwetharani, R. Balakrishna and C. Santoro, *Electrochim. Acta*, 2025, **517**, 145763.
76 F. Ibrahim, K. Kisand, J. Douglin, A. Sarapuu, A. Kikas, M. Kaarik, J. Kozlova, J. Aruväli, A. Treshchalov, J. Leis, V. Kisand, K. Kukli, K. Yassin, D. Dekel and K. Tammeveski, *Chem. Eng. J.*, 2025, **510**, 161560.
77 R. Hao, S. Gu, J. Hu, J. J. Chen, Q. M. Gan, Y. Z. Li, Z. Q. Wang, G. Y. Liu, C. L. Yan, H. M. Yuan, K. Y. Liu, C. Liu and Z. G. Lu, *Carbon*, 2023, **209**, 118031.
78 T. Zierdt, T. Reuter, J. Müller-Hülstede, J. Buschermöhle, D. Schonvogel, J. Kröner, M. Schwan, B. Milow, P. Wagner and K. Friedrich, *ChemSusChem*, 2025, **18**, e202401843.
79 V. Ficca, C. Santoro, E. Placidi, F. Arciprete, A. Serov, P. Atanassov and B. Mecheri, *ACS Catal.*, 2023, **13**, 2162–2175.
80 Z. Cui and X. Bai, *ACS Appl. Mater. Interfaces*, 2022, **14**, 9024–9035.
81 M. E. M. Buan, A. Cognigni, J. C. Walmsley, N. Muthuswamy and M. Ronning, *Catal. Today*, 2020, **357**, 248–258.
82 K. X. Liu, S. Kattel, V. Mao and G. F. Wang, *J. Phys. Chem. C*, 2016, **120**, 1586–1596.
83 W. J. Jiang, L. Gu, L. Li, Y. Zhang, X. Zhang, L. J. Zhang, J. Q. Wang, J. S. Hu, Z. D. Wei and L. J. Wan, *J. Am. Chem. Soc.*, 2016, **138**, 3570–3578.
84 J. H. Zagal and M. T. M. Koper, *Angew. Chem., Int. Ed.*, 2016, **55**, 14510–14521.
85 Y. Hu, J. O. Jensen, C. Pan, L. N. Cleemann, I. Shypunov and Q. F. Li, *Appl. Catal., B*, 2018, **234**, 357–364.
86 Q. Z. Shu, S. X. Yang, X. Y. Zhang, Z. X. Li, Y. Zhang, Y. Tang, H. Gao, C. X. Xia, M. M. Zhao, X. F. Li and H. Zhao, *Int. J. Hydrog. Energy*, 2024, **57**, 90–99.
87 T. Zierdt, M. Bin Mamtaz, T. Eek, J. Müller-Hülstede, S. Rehse, Q. Meyer, D. Schonvogel, P. Wagner, C. Zhao, M. Wark and K. Friedrich, *ChemSusChem*, 2025, **18**, e202500905.
88 G. Bae, M. Kim, M. Han, J. Cho, D. Kim, M. Sougrati, J. Kim, K. Lee, S. Joo, W. Goddard, H. Oh, H. Kim, F. Jaouen and C. Choi, *Nat. Catal.*, 2023, **6**, 1140–1150.
89 T. Zierdt, J. Müller-Hülstede, H. Schmies, D. Schonvogel, P. Wagner and K. A. Friedrich, *ChemElectroChem*, 2024, **11**, e202300583.
90 J. Müller-Hülstede, T. Zierdt, H. Schmies, D. Schonvogel, Q. Meyer, C. Zhao, P. Wagner and M. Wark, *J. Power Sources*, 2022, **537**, 231529.
91 Y. Cheng, M. E. Wang, S. F. Lu, C. J. Tang, X. Wu, J. P. Veder, B. Johannessen, L. Thomsen, J. Zhang, S. Z. Yang, S. Y. Wang and S. P. Jiang, *Appl. Catal., B*, 2021, **284**, 119717.

This journal is © The Royal Society of Chemistry 2026